

Evolution from helical to collinear ferromagnetic order of the Eu^{2+} spins in $\text{RbEu}(\text{Fe}_{1-x}\text{Ni}_x)_4\text{As}_4$

Qianhui Xu,^{1,*} Yi Liu,^{2,3,*} Sijie Hao,^{4,*} Jiahui Qian,⁵ Cheng Su,¹ Chin-Wei Wang,⁶ Thomas Hansen,⁷ Zhendong Fu,⁸ Yixi Su,⁹ Wei Li,⁵ Guang-Han Cao,^{3,†} Yinguo Xiao,^{10,‡} and Wentao Jin^{1,§}

¹*School of Physics, Beihang University, Beijing 100191, China*

²*College of Science, Zhejiang University of Technology, Hangzhou 310023, China*

³*Department of Physics, Zhejiang University, Hangzhou 310027, China*

⁴*Department of Physics, Beijing Normal University, Beijing 100875, China*

⁵*State Key Laboratory of Surface Physics and Department of Physics, Fudan University, Shanghai 200433, China*

⁶*National Synchrotron Radiation Research Center, Hsinchu, 30077, Taiwan*

⁷*Institut Laue-Langevin, BP 156, 38042 Grenoble Cedex 9, France*

⁸*Neutron Platform, Songshan Lake Materials Laboratory, Dongguan 523808, China*

⁹*Jülich Centre for Neutron Science JCNS at Heinz Maier-Leibnitz Zentrum (MLZ),*

Forschungszentrum Jülich GmbH, Lichtenbergstraße 1, D-85747 Garching, Germany

¹⁰*School of Advanced Materials, Peking University Shenzhen Graduate School, Shenzhen 518055, China*

The ground-state magnetic structures of the Eu^{2+} spins in recently discovered $\text{RbEu}(\text{Fe}_{1-x}\text{Ni}_x)_4\text{As}_4$ superconductors have been investigated by neutron powder diffraction measurements. It is found that as the superconductivity gets suppressed with the increase of Ni doping, the magnetic propagation vector of the Eu sublattice diminishes, corresponding to the decrease of the rotation angle between the moments in neighboring Eu layers. The ferromagnetic Eu layers are helically modulated along the c axis with an incommensurate magnetic propagation vector in both the ferromagnetic superconductor $\text{RbEu}(\text{Fe}_{0.95}\text{Ni}_{0.05})_4\text{As}_4$ and the superconducting ferromagnet $\text{RbEu}(\text{Fe}_{0.93}\text{Ni}_{0.07})_4\text{As}_4$. Such a helical structure transforms into a purely collinear ferromagnetic structure for non-superconducting $\text{RbEu}(\text{Fe}_{0.91}\text{Ni}_{0.09})_4\text{As}_4$, with all the Eu^{2+} spins lying along the tetragonal (1 1 0) direction. The evolution from helical to collinear ferromagnetic order of the Eu^{2+} spins with increasing Ni doping is supported by first-principles calculations. The variation of the rotation angle between adjacent Eu^{2+} layers can be well explained by considering the change of magnetic exchange couplings mediated by the indirect Ruderman-Kittel-Kasuya-Yosida (RKKY) interaction.

I. INTRODUCTION

The discovery of iron-based superconductors in 2008 has stimulated worldwide research interests in the investigations of the interplay between magnetism and unconventional superconductivity in these novel materials.^{1,2} Among various members of the iron-based superconductors, the ternary “ EuFe_2As_2 ” (Eu122) system is a unique representative and has attracted much attention, due to the existence of two magnetic sublattices in the unit cell and the strong coupling between spin-, lattice- and charge degrees of freedom.^{3–5} The undoped parent compound EuFe_2As_2 shows an A -type anti-ferromagnetic (AFM) order of the localized Eu^{2+} spins below 19 K, in addition to the spin-density-wave (SDW) order of the itinerant Fe moments below 190 K.^{6,7} By suppressing the SDW order in the Fe sublattice, superconductivity can be achieved by means of chemical substitutions or applying external pressure.^{3,8,9} In the superconducting ground state, single-crystal neutron diffraction or x-ray resonant magnetic scattering experiments have confirmed that strong ferromagnetism from Eu $4f$ orbitals with an ordered moment of $\sim 7 \mu_B$ per Eu atom can coexist microscopically with bulk superconductivity and reach a compromise.^{10–14} The intriguing coexistence of ferromagnetism and superconductivity revealed in the Eu122 system drives the experimental efforts to further explore other novel Eu-containing iron-based superconductors.

In 2016, superconductivity with the transition temperature (T_{SC}) of approximately 31–36 K was discovered in a new family of iron pnictides $\text{CaAFe}_4\text{As}_4$ and $\text{SrAFe}_4\text{As}_4$ ($A = \text{K, Rb, Cs}$) possessing the “1144”-type structure.¹⁵ Later

on, $\text{RbEuFe}_4\text{As}_4$ (denoted as Eu1144 below), crystallizing as an intergrowth structure of heavily hole-doped superconducting RbFe_2As_2 ($T_{SC} = 2.6 \text{ K}$)¹⁶ and non-superconducting EuFe_2As_2 , was reported to be a superconductor as well with $T_{SC} = 36 \text{ K}$.^{17,18} The FeAs layers in Eu1144 are intrinsically hole doped due to the charge homogenization associated with the structural hybridization, which is responsible for the absence of Fe-SDW order and the occurrence of superconductivity. Ascribing to the longer interlayer distance between the Eu layers in Eu1144 compared to Eu122, the Eu^{2+} spins order magnetically at a lower temperature of $T_m = 15 \text{ K}$.

Based on the magnetization and specific heat data obtained from high-quality powder samples, $\text{RbEuFe}_4\text{As}_4$ was speculated to be a ferromagnetic superconductor with a robust coexistence of superconductivity and ferromagnetism.¹⁷ Neutron diffraction measurements on a Eu1144 single crystal have been performed to clarify how the two-dimensional in-plane ferromagnetic Eu layers stack along the c axis.¹⁹ A magnetic propagation vector of $k = (0, 0, 0.25)$ is revealed, suggesting the rotation angle of 90° between the in-plane ferromagnetically aligned Eu^{2+} spins on adjacent layers. Such a helical magnetic structure of undoped Eu1144 is in stark contrast to the collinear A -type AFM structure of undoped EuFe_2As_2 , but resembles those of EuCo_2As_2 and EuNi_2As_2 , showing an incommensurate magnetic propagation vector of $k = (0, 0, 0.79)$ and $k = (0, 0, 0.92)$, respectively.^{20,21}

By introducing extra itinerant electrons via the substitution of Ni^{2+} ($3d^8$) for Fe^{2+} ($3d^6$), the intrinsically doped hole carriers in $\text{RbEuFe}_4\text{As}_4$ can be compensated. Systematic macroscopic characterizations including resistivity,

magnetization, and specific heat measurements have been performed on polycrystalline and single-crystal samples of $\text{RbEu}(\text{Fe}_{1-x}\text{Ni}_x)_4\text{As}_4$ to establish the superconducting and magnetic phase diagram.^{22,23} It is figured out that T_{SC} decreases rapidly with the Ni doping, while the magnetic ordering temperature of the Eu sublattice, T_m , remains essentially unchanged. Consequently, $\text{RbEu}(\text{Fe}_{1-x}\text{Ni}_x)_4\text{As}_4$ transforms from the ferromagnetic superconductor (FSC) with $T_{SC} > T_m$ for $x < 0.07$, to the so-called “superconducting ferromagnet” (SFM) with $T_m > T_{SC}$ for $0.07 \leq x \leq 0.08$, and finally to the ferromagnetic non-superconductor for $x > 0.09$. Furthermore, a recovered Fe-AFM state is proposed for $0.04 \leq x \leq 0.10$ based on the resistivity data on polycrystalline samples.²²

As the helical magnetic order of the Eu^{2+} spins with a two-dimensional (2D) character in undoped $\text{Eu}1144$ is proposed to be associated with the presence of superconductivity,^{24,25} it is of great interest to clarify how the magnetic structure of $\text{RbEu}(\text{Fe}_{1-x}\text{Ni}_x)_4\text{As}_4$ develops against the weakening of the superconductivity induced by Ni doping. Fitting to the magnetic susceptibility in the paramagnetic state yields comparable positive values of Currie-Weiss temperature for samples with different x ,^{22,23} reflecting dominant in-plane ferromagnetic interactions between the Eu^{2+} moments. Detailed neutron diffraction measurements on $\text{RbEu}(\text{Fe}_{1-x}\text{Ni}_x)_4\text{As}_4$ will deliver important information regarding how the stacking pattern of the ferromagnetic Eu layer along the c axis changes with x and how it is correlated with the suppression of superconductivity.

Here we present a systematic study of the magnetic structures of Ni-doped $\text{Eu}1144$ with different doping levels as determined by neutron powder diffraction. We find that as the superconductivity gets suppressed gradually with the increase of Ni doping, the magnetic propagation vector of the Eu sublattice diminishes, corresponding to the decrease of the rotation angle between the moments in neighboring Eu layers. No evidence of the proposed recovery of Fe-SDW order is observed within our experimental resolution. The variation of the rotation angle between adjacent Eu^{2+} layers can be well explained by considering the change of magnetic exchange couplings mediated by the indirect Ruderman-Kittel-Kasuya-Yosida (RKKY) interaction.

II. EXPERIMENTAL DETAILS AND CALCULATION METHODS

Polycrystalline samples of $\text{RbEu}(\text{Fe}_{1-x}\text{Ni}_x)_4\text{As}_4$ ($x = 0.05, 0.07$ and 0.09) of ~ 4 g were synthesized by the solid-state reaction method as described in Ref. 22. The phase purity was checked by x-ray diffraction (XRD) on a PANalytical x-ray diffractometer with a monochromatic $\text{Cu-K}\alpha_1$ radiation. The doping concentration of Ni in three samples was checked by energy-dispersive x-ray spectroscopy (EDS), to be 5.6(6) %, 7.1(8) %, 8.9(5) %, respectively, well consistent with the nominal values. A small amount of FeAs impurity was found to exist in the samples with $x = 0.05$ and 0.07 , and small amounts of RbFe_2As_2 and EuFe_2As_2 impurities were

identified in the sample with $x = 0.09$. Low-temperature neutron powder diffraction (NPD) measurements on the samples with $x = 0.05$ were performed on the high-intensity powder diffractometer Wombat²⁶ at the OPAL facility (Lucas Height, Australia) using incident neutrons with the wavelength of 2.41 \AA and 1.54 \AA , while the data of the sample with $x = 0.07$ were collected using the 1.54 \AA wavelength only. NPD measurements on the sample with $x = 0.09$ were performed on the high-intensity powder diffractometer D20 at Institut Laue-Langevin (Grenoble, France) using incident neutrons with the wavelength of 2.41 \AA and 1.30 \AA . In order to minimize the effect of neutron absorption by the Eu atoms, we have filled the powder samples into the double-wall hollow vanadium cylinder. Refinements of both nuclear and magnetic structures were carried out using the FullProf program suite.²⁷

The first-principles calculations presented in this paper are performed using the projected augmented-wave method,²⁸ as implemented in the VASP code.²⁹ The exchange correlation potential is calculated using the generalized gradient approximation (GGA) as proposed by Perdew, Burke, and Ernzerhof.³⁰ We have included the strong Coulomb repulsion in the Eu-4*f* orbitals on a mean-field level using the GGA+ U_{eff} approximation. Since there exist no spectroscopy data for $\text{RbEu}(\text{Fe}_{1-x}\text{Ni}_x)_4\text{As}_4$, we have used a U_{eff} of 8 eV throughout this work, which is the standard value for an Eu^{2+} ion.^{12,13,31} The results have been checked for consistency with varying U_{eff} values. U_{eff} is not applied to the itinerant Fe-3*d* and Ni-3*d* orbitals. Additionally, the spin-orbit coupling is included for all atoms with the second variational method in the calculations. These calculations are performed using the experimental crystal structure, as determined by the neutron diffraction measurements.

III. RESULTS

The ground-state magnetic structures of the Eu^{2+} spins in $\text{RbEu}(\text{Fe}_{1-x}\text{Ni}_x)_4\text{As}_4$ with different Ni doping levels ($x = 0.05, 0.07$ and 0.09) are determined by NPD measurements and illustrated in Figure 1(b, c, d), together with the helical magnetic structure of undoped $\text{RbEuFe}_4\text{As}_4$ ($x = 0$) with $k = (0, 0, 0.25)$ (Fig. 1(a)) as determined in Ref. 19, which will be discussed in detail below.

Figure 2 shows the NPD patterns of $\text{RbEu}(\text{Fe}_{0.95}\text{Ni}_{0.05})_4\text{As}_4$ at 20 K and 3.9 K. According to the superconducting and magnetic phase diagram of $\text{RbEu}(\text{Fe}_{1-x}\text{Ni}_x)_4\text{As}_4$ deduced from macroscopic measurements in Ref. 22, for this composition, the temperature of 20 K is above T_m ($= 15$ K) but below T_{SDW} ($= 28.9$ K), which is the SDW ordering temperature of Fe. As shown in Fig. 2(a) and 2(c), the diffraction patterns at 20 K can be well fitted with the crystal structure reported in Ref. 22 (space group $P4/mmm$) with a small amount of FeAs impurity (7% wt). Within our experimental uncertainty, no magnetic reflections at $(0.5, 0.5, 3)$ ($Q = 1.84 \text{ \AA}^{-1}$) associated with possible Fe-AFM order can be identified, assuming that the Fe^{2+} moments order in the hedgehog spin-vortex crystal (SVC) motif in each Fe plane and are antiferromagnetically stacked

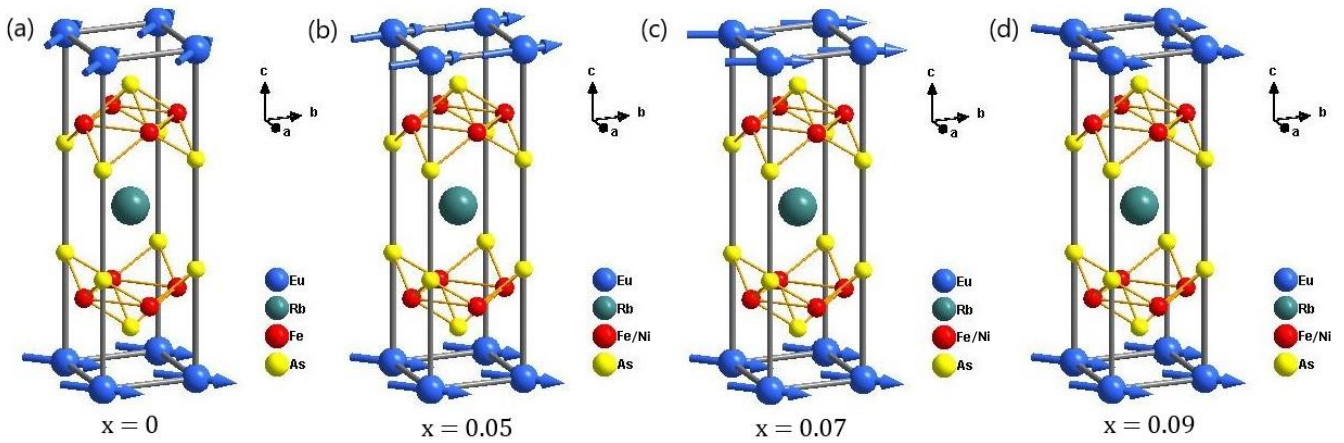


Figure 1: The ground-state magnetic structure of $\text{RbEu}(\text{Fe}_{1-x}\text{Ni}_x)_4\text{As}_4$ with $x = 0$ (a),¹⁹ $x = 0.05$ (b), $x = 0.07$ (c), and $x = 0.09$ (d), in which the rotation angle between the in-plane ferromagnetically aligned Eu^{2+} moments on adjacent layers are 90° , $\sim 49^\circ$, $\sim 26^\circ$, and 0° , respectively.

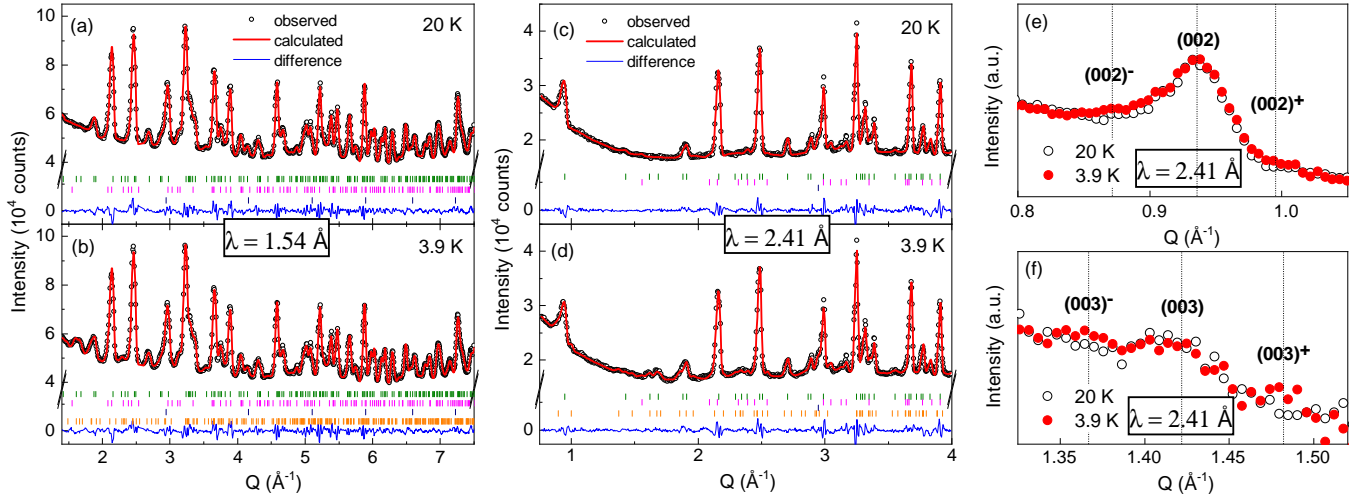


Figure 2: NPD patterns of $\text{RbEu}(\text{Fe}_{0.95}\text{Ni}_{0.05})_4\text{As}_4$ at 20 K (a, c) and 3.9 K (b, d) and the Rietveld refinements. The left (a, b) and right (c-f) panels show the data collected using the incident neutron wavelength of 1.54 Å and 2.41 Å, respectively. The patterns in (b) and (d) are the refinement results obtained by adopting a magnetic structure model with the irreducible representation Γ_5 as described in the text. The circles represent the observed intensities, and the solid lines are the calculated patterns. The differences between the observed and calculated intensities are shown at the bottom. The vertical bars in olive, magenta, navy and orange colors indicate the expected nuclear Bragg reflections from the $\text{RbEu}(\text{Fe}_{0.95}\text{Ni}_{0.05})_4\text{As}_4$ main phase, FeAs impurity, vanadium sample container and the magnetic Bragg reflections from $\text{RbEu}(\text{Fe}_{0.95}\text{Ni}_{0.05})_4\text{As}_4$, respectively. (e) and (f) show the enlarged high-resolution diffraction patterns at 3.9 and 20 K around the (0 0 2) and (0 0 3) nuclear peak positions, respectively, visualizing the incommensurate magnetic satellite reflections appearing at 3.9 K.

along the c direction, similar to that observed in isostructural $\text{CaK}(\text{Fe}_{1-x}\text{Ni}_x)_4\text{As}_4$.^{32,33}

Upon cooling down to 3.9 K, which is well below T_m , the magnetic reflections due to the magnetic ordering of Eu appear as satellite peaks close to the nuclear reflections. As shown in Fig. 2(d), the incident neutron wavelength of $\lambda = 2.41$ Å provides a better resolution at low- Q region, confirming the incommensurate nature of the magnetic peaks. The magnetic reflections at $(0\ 0\ 2)^-/(0\ 0\ 2)^+$ and $(0\ 0\ 3)^-/(0\ 0\ 3)^+$ emerge in both sides of the (0 0 2) and (0 0 3) peaks, as illustrated in Fig. 1(e) and 1(f). Using the k_{search} program integrated in the FullProf suite, the magnetic prop-

agation vector of $k = (0, 0, 0.136(4))$ is figured out for $\text{RbEu}(\text{Fe}_{0.95}\text{Ni}_{0.05})_4\text{As}_4$.

According to the representation analysis performed using the BasReps program also integrated in the FullProf suite (see the supplemental materials for details), for the space group of $P4/mmm$, only two magnetic representations are possible for the Eu ($1a$) site with the propagation vector of $k = (0, 0, 0.136(4))$, which we label as Γ_1 and Γ_5 , respectively. Γ_1 allows the c -axis aligned ferromagnetic Eu layers stacking with modulated moment size values at different layers, which is not consistent with the easy-plane magnetization as revealed from the single-crystal sample with a similar Ni doping level.²³ On

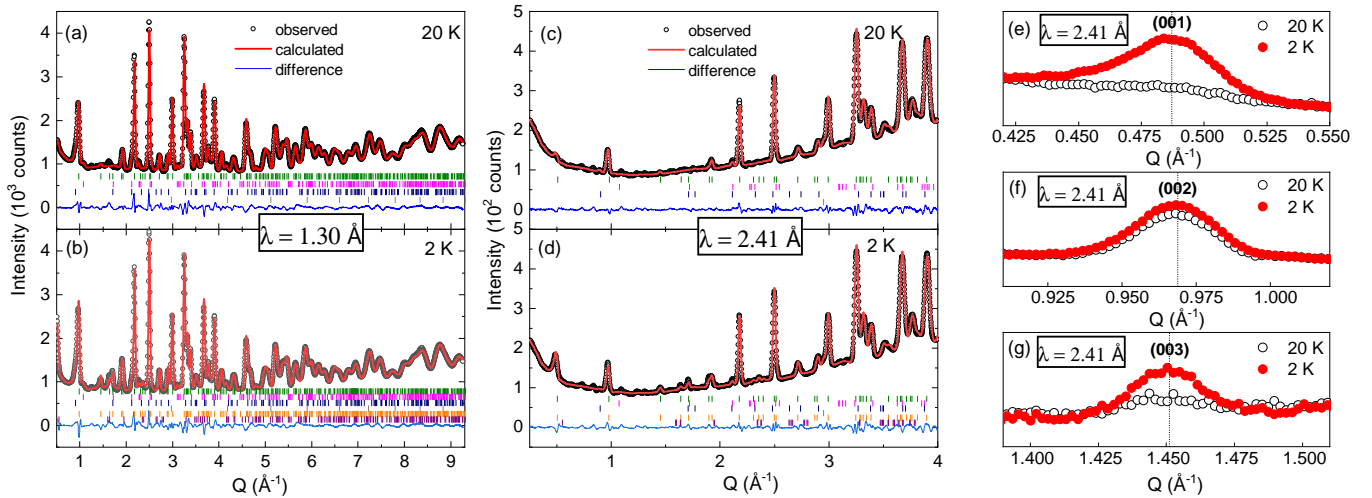


Figure 3: NPD patterns of $\text{RbEu}(\text{Fe}_{0.91}\text{Ni}_{0.09})_4\text{As}_4$ at 20 K (a, c) and 2 K (b, d) and the Rietveld refinements. The left (a, b) and right (c-g) panels show the data collected using the incident neutron wavelength of 1.30 Å and 2.41 Å, respectively. The patterns in (b) and (d) are the refinement results obtained by adopting a magnetic structure model with the irreducible representation Γ_9 as described in the text. The circles represent the observed intensities, and the solid lines are the calculated patterns. The differences between the observed and calculated intensities are shown at the bottom. The vertical bars in olive, magenta, navy, gray, orange and purple colors indicate the expected nuclear Bragg reflections from the $\text{RbEu}(\text{Fe}_{0.91}\text{Ni}_{0.09})_4\text{As}_4$ main phase, EuFe_2As_2 impurity, RbFe_2As_2 impurity, vanadium sample container, as well as the magnetic Bragg reflections from the $\text{RbEu}(\text{Fe}_{0.91}\text{Ni}_{0.09})_4\text{As}_4$ main phase and the EuFe_2As_2 impurity, respectively. (e), (f) and (g) show the enlarged high-resolution diffraction patterns at 2 and 20 K around the (0 0 1), (0 0 2) and (0 0 3) nuclear peak positions, respectively, illustrating the commensurate magnetic contributions with $k = 0$ at 2 K.

the other hand, Γ_5 allows the in-plane aligned ferromagnetic Eu layers to stack helically along the c axis, with a constant moment size value at different layers. This model fits pretty well to the diffraction patterns at 3.9 K, as shown by the solid curves in Fig. 2(b) and 2(d). As a comparison between the fitting using Γ_5 and Γ_1 , Fig. S2 in the supplemental materials shows a better agreement of Γ_5 with the observed intensities in the very low- Q region, where the magnetic form factor dominates. The nuclear structure parameters and the scale factor derived from the refinement of 20 K data was fixed in the refinement of 3.9 K data to derive the moment size of Eu to be $6.3(2) \mu_B$, as listed in Table 1. As illustrated in Fig. 1(b), the Eu^{2+} moments form an incommensurate helical structure, with the moment direction lying in the ab plane but rotating by $\sim 49^\circ$ around the c axis with respect to adjacent Eu layers. Using the Bilbao Crystallographic Server,³⁴ the magnetic space group of this helical structure is determined to be $Pm'm'm$ (No. 47.252).

Figure 3 shows the NPD patterns of $\text{RbEu}(\text{Fe}_{0.91}\text{Ni}_{0.09})_4\text{As}_4$ at 20 K and 2 K. This sample is non-superconducting as evidenced from previous macroscopic characterizations.²² It undergoes the magnetic ordering of Eu sublattice at T_m ($= 14.7$ K) and a possible recovered Fe-SDW ordering at T_{SDW} ($= 31.3$ K). Similar to the case of $x = 0.5$ presented above, no visible change of intensities at $(0.5, 0.5, 1)$ ($Q = 1.25 \text{ \AA}^{-1}$) and $(0.5, 0.5, 3)$ ($Q = 1.84 \text{ \AA}^{-1}$) associated with the Fe-AFM order can be resolved at 20 K compared with 40 K (data of which is not shown). The diffraction patterns at 20 K can be well fitted using the nuclear crystal structure in the space group of $P4/mmm$,

together with small amount impurities phases of RbFe_2As_2 (6.2% wt) and EuFe_2As_2 (4.4% wt), as shown in Fig. 3(a) and 3(c).

In stark contrast to the magnetic satellite peaks displayed in $\text{RbEu}(\text{Fe}_{0.95}\text{Ni}_{0.05})_4\text{As}_4$ arising from the helical magnetic structure of Eu, here at 2 K, well below T_m , the magnetic scatterings due to the ordering of Eu^{2+} spins appear on top of the nuclear reflections for $\text{RbEu}(\text{Fe}_{0.91}\text{Ni}_{0.09})_4\text{As}_4$, which is shown in Fig. 3(e-g) for $Q = (0 0 1)$ (e), $(0 0 2)$ (f) and $(0 0 3)$ (g) measured with a high resolution using $\lambda = 2.41 \text{ \AA}$. This clearly indicates a magnetic propagation vector of $k = 0$.

Magnetic representation analysis for $k = 0$ for the space group of $P4/mmm$ yields only two possible irreducible representations for the $\text{Eu}(1a)$ site (see the supplemental materials for details), labeled as Γ_8 and Γ_9 , respectively. They correspond to the collinear ferromagnetic structures in which all the Eu^{2+} moments are aligned along the c axis and in the ab plane, respectively. Although no magnetization data on single-crystal $\text{RbEu}(\text{Fe}_{0.91}\text{Ni}_{0.09})_4\text{As}_4$ is available, the moment direction of Eu^{2+} spins can still be identified according to the nature of magnetic neutron diffraction. As the magnetic scattering is only sensitive to the component of the moment perpendicular to Q , dramatic enhancements of intensities of $(0 0 L)$ peaks and no visible changes of $(H K 0)$ peak intensities suggest that the Eu^{2+} moments are mostly lying in the ab plane so that the magnetic structure model described by Γ_8 can be excluded. Indeed the Γ_9 model with all spins aligned along in-plane $(1 1 0)$ direction fits the diffraction patterns at 2 K quite well, as shown by the solid curves in Fig. 3(b) and 3(d). As the fraction of the EuFe_2As_2 impurity phase is quite

Table 1: Refined results for the nuclear and magnetic structure parameters of $\text{RbEu}(\text{Fe}_{1-x}\text{Ni}_x)_4\text{As}_4$ with $x = 0.05, 0.07$ and 0.09 . The atomic positions are as follows: Eu, $1a$ (0, 0, 0); Rb, $1d$ (0.5, 0.5, 0.5); Fe/Ni, $4i$ (0, 0.5, z_{Fe}); As1, $2g$ (0, 0, z_{As1}); As2, $2h$ (0.5, 0.5, z_{As2}). The occupancies of Fe and Ni were fixed according to the nominal compositions, respectively. The nuclear structure parameters and the scale factor derived from the refinement of 20 K data was fixed in the magnetic-structure refinements (Space group: $P4/mmm$)

Composition		$\text{RbEu}(\text{Fe}_{0.95}\text{Ni}_{0.05})_4\text{As}_4$		$\text{RbEu}(\text{Fe}_{0.93}\text{Ni}_{0.07})_4\text{As}_4$		$\text{RbEu}(\text{Fe}_{0.91}\text{Ni}_{0.09})_4\text{As}_4$	
Temperature		20 K	3.9 K	20 K	3.3 K	20 K	2 K
Eu	B_{iso} (\AA^2)	1.3(1)	-	1.2(1)	-	0.22(5)	-
	M (μ_B)	-	6.3(2)	-	6.3(2)	-	6.5(1)
Rb	B_{iso} (\AA^2)	1.4(1)	-	1.3(1)	-	1.1(1)	-
Fe/Ni	z_{Fe}	0.2309(2)	-	0.2310(2)	-	0.2315(1)	-
	B_{iso} (\AA^2)	1.0(1)	-	0.8(1)	-	0.26(1)	-
As1	z_{As1}	0.3344(4)	-	0.3339(4)	-	0.3339(2)	-
	B_{iso} (\AA^2)	1.1(1)	-	0.8(1)	-	0.24(3)	-
As2	z_{As2}	0.1263(4)	-	0.1263(4)	-	0.1277(2)	-
	B_{iso} (\AA^2)	1.3(1)	-	0.8(1)	-	0.24(3)	-
a (\AA)		3.8652(4)	3.8651(2)	3.8649(5)	3.8646(2)	3.8921(3)	3.8920(2)
c (\AA)		13.117(2)	13.117(1)	13.109(2)	13.108(1)	13.218(1)	13.216(1)
R_{F2}		1.29	1.28	1.31	1.34	1.86	2.01
R_{wF2}		1.73	1.72	1.83	1.86	2.40	2.63
R_F		0.43	0.44	0.42	0.43	0.36	0.36

small (4.4% wt), including the its magnetic phase in the refinement has no visible effect on the fitting of the 2 K data and the results about the 1144 main phase. Fixing the nuclear structure parameters and the scale factor derived from the refinement of 20 K data, the refinement of 2 K data yields the moment size of Eu to be $6.5(1) \mu_B$ (see Table 1). Please note that a lower saturated moment of $6.0 \mu_B/\text{Eu}$ for $x = 0.09$ in Ref. 22 is because of some nonmagnetic Eu_2O_3 impurities forming in older samples due to oxidation of metallic Eu. In fact, the saturated moment of Eu^{2+} spins should be independent of the Ni doping level. The magnetic structure of $\text{RbEu}(\text{Fe}_{0.91}\text{Ni}_{0.09})_4\text{As}_4$ is illustrated in Fig. 1(d). Compared with the undoped $\text{Eu}1144$ and $\text{RbEu}(\text{Fe}_{0.95}\text{Ni}_{0.05})_4\text{As}_4$ with $x = 0.05$, the rotation angle between the moments in neighboring Eu layers diminishes to zero for $\text{RbEu}(\text{Fe}_{0.91}\text{Ni}_{0.09})_4\text{As}_4$ with $x = 0.09$, forming a collinear in-plane ferromagnetic structure. The magnetic space group of this helical structure is determined to be $Cmm'm'$ (No. 65.486).

After presenting the results of $\text{RbEu}(\text{Fe}_{1-x}\text{Ni}_x)_4\text{As}_4$ with $x = 0.05$ and 0.09 , we come to the magnetic structure determination of the SFM $\text{RbEu}(\text{Fe}_{0.93}\text{Ni}_{0.07})_4\text{As}_4$ ($T_{SC} = 11.2$ K) with T_m and T_{SDW} being 15.1 K and 35.0 K, respectively.²² As shown in Fig. 4(a), the diffraction pattern of $\text{RbEu}(\text{Fe}_{0.93}\text{Ni}_{0.07})_4\text{As}_4$ at 20 K can be well fitted with the nuclear crystal structure in the space group of $P4/mmm$ together with a small amount impurities phase of FeAs (5.9% wt). Again, no magnetic peaks at (0.5, 0.5, 3) arising from the Fe-AFM order can be identified. Upon cooling down to the base temperature of 3.3 K, the magnetic scattering due to magnetic ordering of Eu^{2+} spins sets in. Unfortunately the high-resolution datasets with $\lambda = 2.41 \text{ \AA}$ is lacking for this sample, due to the limited neutron beamtime. However, by setting the magnetic propagation vector k itself as a variable parameter in the refinement of 3.3 K data, the diffraction pattern can be fitted pretty well with k finally converged to (0, 0, 0.071(7)) and the moment size of Eu^{2+} spins being $6.3(2) \mu_B$, as shown

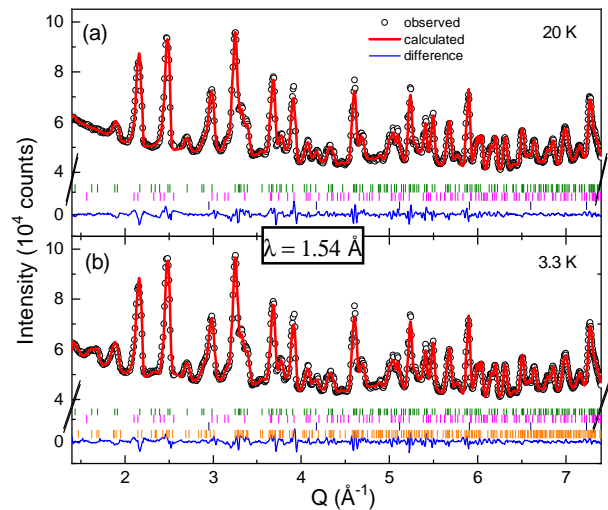


Figure 4: NPD patterns of $\text{RbEu}(\text{Fe}_{0.93}\text{Ni}_{0.07})_4\text{As}_4$ at 20 K (a) and 3.3 K (b) collected using the incident neutron wavelength of 1.54 \AA and the Rietveld refinements. The pattern in (b) is the refinement result obtained by adopting a magnetic structure model with the irreducible representation Γ_5 as described in the text. The circles represent the observed intensities, and the solid lines are the calculated patterns. The differences between the observed and calculated intensities are shown at the bottom. The vertical bars in olive, magenta, navy and orange colors indicate the expected nuclear Bragg reflection from $\text{RbEu}(\text{Fe}_{0.93}\text{Ni}_{0.07})_4\text{As}_4$, FeAs impurity, vanadium sample container and the magnetic Bragg reflection from $\text{RbEu}(\text{Fe}_{0.93}\text{Ni}_{0.07})_4\text{As}_4$, respectively.

in Table 1 and Fig. 4(b). This result corresponds to a helical magnetic structure similar to that of $\text{RbEu}(\text{Fe}_{0.95}\text{Ni}_{0.05})_4\text{As}_4$, but with a smaller helix rotation angle of $\sim 26^\circ$.

Using first-principles calculations, the energetic properties of different spin configurations of the Eu^{2+} moments are com-

Table 2: Energetic properties of the different spin configurations of the Eu^{2+} moments for $\text{RbEuFe}_4\text{As}_4$. The results are the total energy difference per Eu atom. The helical, antiparallel and parallel configurations correspond to the magnetic structures in which the in-plane ferromagnetic Eu^{2+} moments on adjacent layers are vertical, antiparallel, and parallel, respectively.

configurations	$\Delta E(\text{meV})$	$M_{\text{Eu}}(\mu_B)$
helical ($k = (0, 0, 0.25)$)	0	6.986
antiparallel	49.71	6.962
parallel	49.21	6.962

Table 3: Energetic properties of the different spin configurations of the Eu^{2+} moments for $\text{RbEu}(\text{Fe}_{0.875}\text{Ni}_{0.125})_4\text{As}_4$. The results are the total energy difference per Eu atom. The helical, antiparallel and parallel configurations correspond to the magnetic structures in which the in-plane ferromagnetic Eu^{2+} moments on adjacent layers are vertical, antiparallel, and parallel, respectively.

configurations	$\Delta E(\text{meV})$	$M_{\text{Eu}}(\mu_B)$
helical ($k = (0, 0, 0.25)$)	0	6.971
antiparallel	2.01	6.965
parallel	-2.04	6.970

puted for $\text{RbEuFe}_4\text{As}_4$ and $\text{RbEu}(\text{Fe}_{0.875}\text{Ni}_{0.125})_4\text{As}_4$, respectively. As shown in Table 2 and 3, it is found that the noncollinear helical structure with $k = (0, 0, 0.25)$ possesses the lowest energy for the parent compound $\text{RbEuFe}_4\text{As}_4$, while the collinear ferromagnetic structure with the Eu^{2+} moments lying in the ab plane is energetically favorable for $\text{RbEu}(\text{Fe}_{0.875}\text{Ni}_{0.125})_4\text{As}_4$ with $x = 0.125$. These are well consistent with our experimental findings that the rotation angle between the moments in neighboring Eu layers diminishes with increasing Ni doping and the helical structure finally transforms into a purely collinear ferromagnetic structure.

IV. DISCUSSION AND CONCLUSION

As shown in Fig. 1, the magnetic structure of the Eu^{2+} moments in $\text{RbEu}(\text{Fe}_{1-x}\text{Ni}_x)_4\text{As}_4$ undergoes a smooth evolution from the helical structure, in which the in-plane ferromagnetically aligned Eu^{2+} spins on adjacent layers rotate by 90° , gradually to a collinear ferromagnetic structure, in which all the Eu^{2+} spins point along the tetragonal (1 1 0) direction. The c -component of the magnetic propagation vector, k_z , and the helix rotation angle (θ) are plotted in Fig. 5(a) and 5(b) as a function of the Ni content x , respectively. Both of them diminish with increasing Ni content, in accordance with the gradual suppression of superconductivity as reported in Ref. 22.

It was reported recently that in isostructural $\text{CaK}(\text{Fe}_{1-x}\text{Ni}_x)_4\text{As}_4$, the Ni doping may lead to the emergence of a hedgehog-type spin-vortex crystal (SVC) order of the Fe moments,^{32,33} which is different from the stripe-type Fe-SDW order observed in “122” family iron pnictides.^{2,7,35} However, within our experimental resolution,

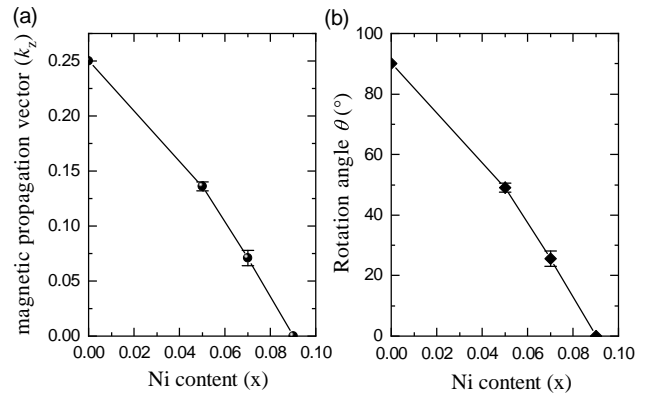


Figure 5: The evolution of magnetic propagation vector $k = (0, 0, k_z)$ (a) and the rotation angle (θ) of the Eu^{2+} spins between adjacent Eu layers (b) in $\text{RbEu}(\text{Fe}_{1-x}\text{Ni}_x)_4\text{As}_4$ as a function of the Ni content x .

the proposed recovery of Fe-AFM order with Ni doping can not be identified at $Q = (0.5, 0.5, L)$ ($L = \text{integers}$), probably due to the weakness of related magnetic reflections from small Fe^{2+} moments and high background in the NPD measurements. Future neutron diffraction experiments on large single-crystal samples of $\text{RbEu}(\text{Fe}_{1-x}\text{Ni}_x)_4\text{As}_4$, if available, will be crucial to confirm the possibly restored antiferromagnetism in the Fe sublattice.

The variation of the magnetic structure of Eu in $\text{RbEu}(\text{Fe}_{1-x}\text{Ni}_x)_4\text{As}_4$ can be understood semi-quantitatively in consideration of the exchange couplings. As the magnetism of Eu in Eu1144 is believed to be of a 2D character, the helix rotation angle θ between the ferromagnetic Eu^{2+} layers predominantly depend on the competition between the nearest (J_{c1}) and next-nearest (J_{c2}) interlayer couplings (see Fig. 6(a)), with $\cos\theta = -\frac{J_{c1}}{4J_{c2}}$.³⁶ These exchange couplings between interlayer Eu^{2+} moments is realized through the indirect Ruderman-Kittel-Kasuya-Yosida (RKKY) interaction J_{RKKY} , mediated by the conduction d electrons on the FeAs layers, in the form of $J_c \propto J_{\text{RKKY}}\cos(2k_F r)/r^3$, where r denotes the interlayer distance between the Eu^{2+} moments and k_F is the Fermi vector.³⁷⁻⁴⁰ Using first-principles calculations, it is figured out that the RKKY interaction strength J_{RKKY} is isotropic and barely changed upon Ni-doping (~ 0.12 meV).⁴¹ In the undoped Eu1144, J_{c1} is expected to be zero (for $\theta = 90^\circ$ and $\cos\theta = 0$), consistent with the 2D character of the Eu magnetism. This corresponds to $2k_F r_0 = (2n+1)\pi/2$, with k_F and r_0 being the Fermi vector and nearest interlayer distance between the Eu^{2+} moments without Ni doping. $J_{c2} \propto J_{\text{RKKY}}\cos(4k_F r_0)/(2r_0)^3$ is therefore negative, responsible for the antiferromagnetic next-nearest interlayer coupling. As the hole carriers are compensated by the substitution of Ni^{2+} ($3d^8$) for Fe^{2+} ($3d^6$), the Fermi vector k_F shrinks effectively, leading to the decrease of $k_F r$. Therefore, $|J_{c1}|$ increases and $|J_{c2}|$ decreases as the value of $k_F r$ is tuned away from $(n+1/2)\pi$, resulting in the increase of $\cos\theta$ ($= -\frac{J_{c1}}{4J_{c2}}$) and the decrease of θ , as shown in Fig. 6(b) and its inset. This well explains the gradual disappearance of rela-

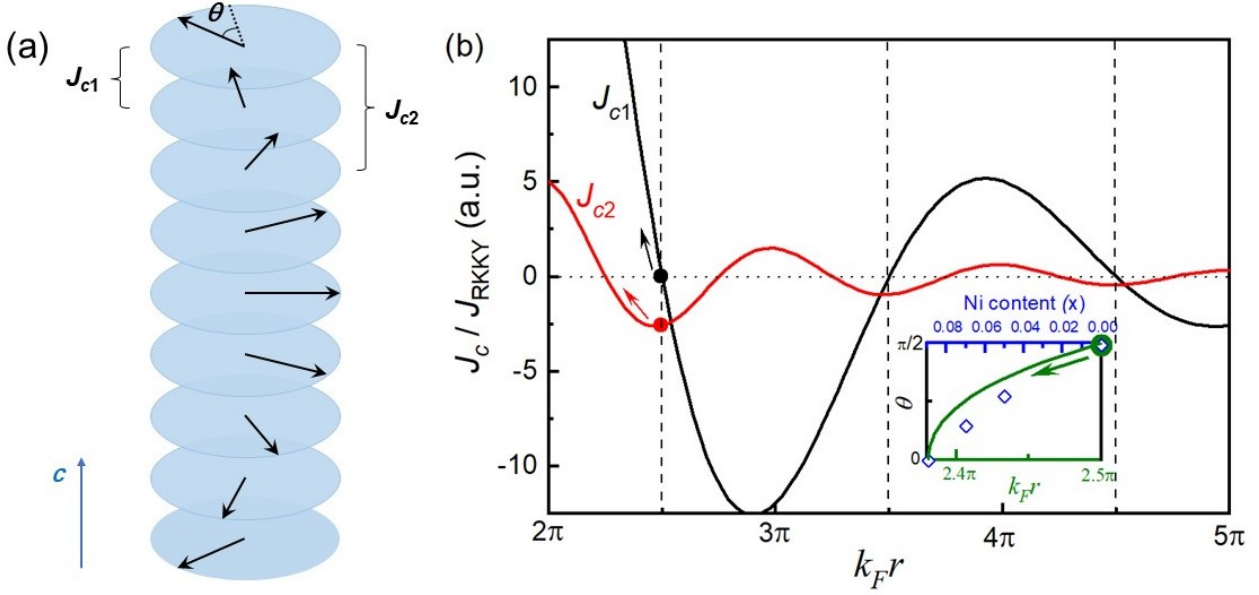


Figure 6: An illustration of the spin directions in different layers of the helical magnetic structure (a) and a semi-quantitative description of the interlayer couplings as well as the rotation angle θ in the helix as a function of $k_F r$ (b). The nearest (J_{c1} , black solid line) and next-nearest (J_{c2} , red solid line) interlayer couplings are assumed to be in the form of $J_{c1} = C J_{\text{RKKY}} \cos(2k_F r)/r^3$ and $J_{c2} = C J_{\text{RKKY}} \cos(4k_F r)/(2r)^3$, respectively, where C is a scaling constant. The helix rotation angle θ (in the inset) is then calculated using $\cos\theta = -J_{c1}/4J_{c2}$. The vertical dashed lines in (b) mark the possible $k_F r$ values of undoped Eu1144, where $J_{c1} = 0$ and $J_{c2} < 0$. Assuming that for undoped Eu1144 $k_F r = 2.5\pi$, the black, red, and olive arrows next to the corresponding solid circles represent the shifts of J_{c1} , J_{c2} , and θ values with the decrease of $k_F r$ induced by Ni doping. The blue diamonds in the inset of (b) represent the θ values for different Ni content x determined experimentally as shown in Fig. 5(b) for comparison.

tive rotation between adjacent Eu^{2+} layers with increasing Ni doping as determined experimentally.

It is argued that the emergence of helical magnetic structure with a period of four unit cells along the c axis in undoped Eu1144 ($k = (0, 0, 0.25)$) is favored by the exchange interaction between superconductivity and ferromagnetism,²⁴ as predicted by Anderson and Suhl long time ago to be one solution for the compromise between these two antagonistic phenomena.⁴² As an alternate scenario, it is proposed theoretically that the ferromagnetic contribution to the interlayer RKKY interaction from the non-superconducting normal parts and the antiferromagnetic contribution from the superconducting layers compete with each other, giving rise to the helical ground-state magnetic configuration as a result of frustration.²⁵ It is worth pointing out that our experimental results are also qualitatively consistent with these arguments. On one hand, the helix rotation angle θ diminishes with Ni doping, thus releasing the frustration in favor of a collinear ferromagnetic structure. On the other hand, according to the prediction by Anderson and Suhl, the periodicity of the spin helix d is correlated with the superconducting coherence length ξ_0 in the form of $d \propto (\xi_0)^{1/3}$.⁴² As the superconducting transition temperature T_{SC} and the upper critical field H_{c2} decrease with increasing Ni doping,²³ ξ_0 increases according to the Ginzburg-Landau formalism $H_{c2} = \Phi_0/2\pi\xi_0^2$, which is consistent with the diminishing θ and increasing helix periodicity d . Although some recent spectroscopic measurements seem to suggest the decoupling of magnetism from Eu from

superconducting FeAs layers,^{43,44} we note that a recent scanning Hall microscopy experiment has revealed a pronounced suppression of the superfluid density near the Eu magnetic ordering temperature in Eu1144, indicating a pronounced exchange interaction between the superconducting and magnetic subsystems.⁴⁵

In conclusion, the magnetic structures of $\text{RbEu}(\text{Fe}_{1-x}\text{Ni}_x)_4\text{As}_4$ superconductors are systematically investigated by neutron powder diffraction. It is found that as the superconductivity gets suppressed gradually with the increase of Ni doping, the magnetic propagation vector of the Eu sublattice diminishes, corresponding to the decrease of the rotation angle between the moments in neighboring Eu layers with a helical structure. For non-superconducting $\text{RbEu}(\text{Fe}_{0.91}\text{Ni}_{0.09})_4\text{As}_4$, all the Eu^{2+} spins point along the tetragonal (1 1 0) direction, forming a purely collinear ferromagnetic structure. Such an evolution from helical to collinear ferromagnetic order of the Eu^{2+} spins with increasing Ni doping is well supported by first-principles calculations. The variation of the rotation angle between adjacent Eu^{2+} layers can be well explained by considering the change of magnetic exchange couplings mediated by the indirect RKKY interaction.

Acknowledgments

This work is partly based on experiments performed at the Australian Nuclear Science and Technology Organisation (ANSTO), Sydney, Australia and the Institut Laue-Langevin (ILL), Grenoble, France. W.T.J. would like to acknowledge Shang Gao, Hao Deng and Karen Friese for helpful discussions. The authors acknowledge the supports by the National

Natural Science Foundation of China (Grant No. 12074023 and 11927807), the National Key Research and Development Program of China (2016YFA0300202), the Fundamental Research Funds for the Central Universities in China (YWF-20-BJ-J-1043 and YWF-21-BJ-J-1044), and Shanghai Science and Technology Committee (Grant Nos. 19ZR1402600 and 20DZ1100604).

-
- * These authors contributed equally to this work.
[†] Electronic address: ghcao@zju.edu.cn
[‡] Electronic address: y.xiao@pku.edu.cn
[§] Electronic address: wtjin@buaa.edu.cn
- ¹ Y. Kamihara, T. Watanabe, M. Hirano, and H. Hosono, *J. Am. Chem. Soc.* **130**, 3296 (2008).
 - ² P. Dai, *Rev. Mod. Phys.* **87**, 855 (2015).
 - ³ S. Zapf and M. Dressel, *Rep. Prog. Phys.* **80**, 016501 (2017).
 - ⁴ Y. Xiao, Y. Su, W. Schmidt, K. Schmalzl, C. M. N. Kumar, S. Price, T. Chatterji, R. Mittal, L. J. Chang, S. Nandi, et al., *Phys. Rev. B (R)* **81**, 220406 (2010).
 - ⁵ Y. Xiao, Y. Su, S. Nandi, S. Price, B. Schmitz, C. M. N. Kumar, R. Mittal, T. Chatterji, N. Kumar, S. K. Dhar, et al., *Phys. Rev. B* **85**, 094504 (2012).
 - ⁶ Z. Ren, Z. Zhu, S. Jiang, X. Xu, Q. Tao, C. Wang, C. Feng, G. Cao, and Z. Xu, *Phys. Rev. B* **78**, 052501 (2008).
 - ⁷ Y. Xiao, Y. Su, M. Meven, R. Mittal, C. M. N. Kumar, T. Chatterji, S. Price, J. Persson, N. Kumar, S. K. Dhar, et al., *Phys. Rev. B* **80**, 174424 (2009).
 - ⁸ Z. Ren, Q. Tao, S. Jiang, C. Feng, C. Wang, J. Dai, G. Cao, and Z. Xu, *Phys. Rev. Lett.* **102**, 137002 (2009).
 - ⁹ C. F. Miclea, M. Nicklas, H. S. Jeevan, D. Kasinathan, Z. Hossain, H. Rosner, P. Gegenwart, C. Geibel, and F. Steglich, *Phys. Rev. B* **79**, 212509 (2009).
 - ¹⁰ W. T. Jin, S. Nandi, Y. Xiao, Y. Su, O. Zaharko, Z. Guguchia, Z. Bukowski, S. Price, W. H. Jiao, G. H. Cao, et al., *Phys. Rev. B* **88**, 214516 (2013).
 - ¹¹ S. Nandi, W. T. Jin, Y. Xiao, Y. Su, S. Price, D. K. Shukla, J. Stempfer, H. S. Jeevan, P. Gegenwart, and T. Brückel, *Phys. Rev. B* **89**, 014512 (2014).
 - ¹² W. T. Jin, W. Li, Y. Su, S. Nandi, Y. Xiao, W. H. Jiao, M. Meven, A. P. Sazonov, E. Feng, Y. Chen, et al., *Phys. Rev. B* **91**, 064506 (2015).
 - ¹³ Z. Zhou, W. T. Jin, W. Li, S. Nandi, B. Ouladdiaf, Z. Yan, X. Wei, X. Xu, W. H. Jiao, N. Qureshi, et al., *Phys. Rev. B* **100**, 060406(R) (2019).
 - ¹⁴ W. T. Jin, J. P. Sun, G. Z. Ye, Y. Xiao, Y. Su, K. Schmalzl, S. Nandi, Z. Bukowski, Z. Guguchia, E. Feng, et al., *Sci. Rep.* **7**, 3532 (2017).
 - ¹⁵ A. Iyo, K. Kawashima, T. Kinjo, T. Nishio, S. Ishida, H. Fujihisa, Y. Gotoh, K. Kihou, H. Eisaki, and Y. Yoshida, *J. Am. Chem. Soc.* **138**, 3410 (2016).
 - ¹⁶ Z. Bukowski, S. Weyeneth, R. Puzniak, J. Karpinski, and B. Batlogg, *Physica C* **470**, S328 (2010).
 - ¹⁷ Y. Liu, Y.-B. Liu, Z.-T. Tang, H. Jiang, Z.-C. Wang, A. Ablimit, W.-H. Jiao, Q. Tao, C.-M. Feng, Z.-A. Xu, et al., *Phys. Rev. B* **93**, 214503 (2016).
 - ¹⁸ M. P. Smylie, K. Willa, J.-K. Bao, K. Ryan, Z. Islam, H. Claus, Y. Simsek, Z. Diao, A. Rydh, A. E. Koshelev, et al., *Phys. Rev. B* **98**, 104503 (2018).
 - ¹⁹ K. Iida, Y. Nagai, S. Ishida, M. Ishikado, N. Murai, A. D. Christianson, H. Yoshida, Y. Inamura, H. Nakamura, A. Nakao, et al., *Phys. Rev. B* **100**, 014506 (2019).
 - ²⁰ X. Tan, G. Fabbris, D. Haskel, A. A. Yaroslavlsev, H. Cao, C. M. Thompson, K. Kovnir, A. P. Menushenkov, R. V. Chernikov, V. Ovidiu Garlea, et al., *J. Am. Chem. Soc.* **138**, 2724 (2016).
 - ²¹ W. T. Jin, N. Qureshi, Z. Bukowski, Y. Xiao, S. Nandi, M. Babij, Z. Fu, Y. Su, and T. Brückel, *Phys. Rev. B* **99**, 014425 (2019).
 - ²² Y. Liu, Y.-B. Liu, Y.-L. Yu, Q. Tao, C.-M. Feng, and G.-H. Cao, *Phys. Rev. B* **96**, 224510 (2017).
 - ²³ K. Willa, M. P. Smylie, Y. Simsek, J.-K. Bao, D. Y. Chung, M. G. Kanatzidis, W.-K. Kwok, and U. Welp, *Phys. Rev. B* **101**, 064508 (2020).
 - ²⁴ Z. Devizorova and A. Buzdin, *Phys. Rev. B* **100**, 104523 (2019).
 - ²⁵ A. E. Koshelev, *Phys. Rev. B* **100**, 224503 (2019).
 - ²⁶ A. J. Studer, M. E. Hagen, and T. J. Noakes, *Physica B: Condensed Matter* **385-386**, 1013 (2006).
 - ²⁷ J. Rodriguez-Carvajal, *Physica B* **192**, 55 (1993).
 - ²⁸ P. E. Blöchl, *Phys. Rev. B* **50**, 17953 (1994).
 - ²⁹ G. Kresse and J. Furthmüller, *Phys. Rev. B* **54**, 11169 (1996).
 - ³⁰ J. P. Perdew, K. Burke, and M. Ernzerhof, *Phys. Rev. Lett.* **77**, 3865 (1996).
 - ³¹ W. Li, J. X. Zhu, Y. Chen, and C. S. Ting, *Phys. Rev. B* **86**, 155119 (2012).
 - ³² W. R. Meier, Q.-P. Ding, A. Kreyssig, S. L. Bud'ko, A. Sapkota, K. Kothapalli, V. Borisov, R. Valentí, C. D. Batista, P. P. Orth, et al., *npj Quant. Mater.* **3**, 5 (2018).
 - ³³ A. Kreyssig, J. M. Wilde, A. E. Böhmer, W. Tian, W. R. Meier, B. Li, B. G. Ueland, M. Xu, S. L. Bud'ko, P. C. Canfield, et al., *Phys. Rev. B* **97**, 224521 (2018).
 - ³⁴ M. I. Aroyo, J. M. Perez-Mato, D. Orobengoa, E. Tasci, G. de la Flor, A. Kirov, *Bulg. Chem. Commun.* **43**, 183 (2011).
 - ³⁵ Y. Su, P. Link, A. Schneidewind, T. Wolf, P. Adelman, Y. Xiao, M. Meven, R. Mittal, M. Rotter, D. Johrendt, et al., *Phys. Rev. B* **79**, 064504 (2009).
 - ³⁶ Stephen Blundell, *Magnetism in Condensed Matter*, Oxford University Press, 2001.
 - ³⁷ M. A. Ruderman, and C. Kittel, *Phys. Rev.* **96**, 99 (1954).
 - ³⁸ T. Kasuya, *Progr. Theor. Phys.* **16**, 45 (1956).
 - ³⁹ K. Yosida, *Phys. Rev.* **106**, 893 (1957).
 - ⁴⁰ A. Akbari, P. Thalmeier, and I. Eremin, *New J. Phys.* **15**, 033034 (2013).
 - ⁴¹ C. Xu, Q. Chen, and C. Cao, *Commun. Phys.* **2**, 16 (2019).
 - ⁴² P. W. Anderson and H. Suhl, *Phys. Rev.* **116**, 898 (1959).
 - ⁴³ M. Hemmida, N. Winterhalter-Stocker, D. Ehlers, H.-A. K. von Nidda, M. Yao, J. Bannier, E. D. L. Rienks, R. Kurlito, C. Felser, B. Büchner, et al., *Phys. Rev. B* **103**, 195112 (2021).
 - ⁴⁴ T. K. Kim, K. S. Pervakov, D. V. Evtushinsky, S. W. Jung, G. Poelchen, K. Kummer, V. A. Vlasenko, A. V. Sadakov, A. S. Usoltsev, V. M. Pudalov, et al., *Phys. Rev. B* **103**, 174517 (2021).

⁴⁵ D. Collomb, S. J. Bending, A. E. Koshelev, M. P. Smylie, L. Farrar, J.-K. Bao, D. Y. Chung, M. G. Kanatzidis, W.-K. Kwok, and

U. Welp, Phys. Rev. Lett. **126**, 157001 (2021).